Passive-ocean radial basis function approach to improve temporal gravity recovery from GRACE observations

Fan Yang[1,2]**, Jürgen Kusche**[2]**, Ehsan Forootan**[3]**, and Roelof Rietbroek**[2]

[1]School of Physics, Huazhong University of Science and Technology, Wuhan, China

[2]Institute of Geodesy and Geoinformation, University of Bonn, Bonn, Germany

[3]School of Earth and Ocean Science, Cardiff University, Cardiff, United Kingdom

Key Points:

- Radial basis function approach for GRACE gravity recovery
- Accounting for the passive ocean response in the gravity recovery
- More accurate coastal gravity modelling

Corresponding author: Fan Yang, `mrfanyang90@gmail.com`

Abstract

We present a new state-of-the-art of passive-ocean Modified Radial Basis Functions (MRBFs) that improves the recovery of time-variable gravity fields from GRACE. As is well known, spherical harmonics (SHs), which are commonly used to estimate GRACE level 2 gravity field products, are orthogonal basis functions with global coverage. However, the chosen SH truncation involves a global compromise between data coverage and obtainable resolution, and strong localized signals, such as melting glaciers, may not be fully captured. Radial basis functions (RBFs) provide another representation, which has been proposed in earlier works as being better suited to retrieve regional gravity signals. In this paper, we propose a MRBF approach by embedding the known coastal geometries in the RBF parameterization and imposing global mass conservation and equilibrium behavior of the oceans. Our hypothesis is that, with this physically justified constraint, the GRACE-derived gravity signals can be more realistically partitioned into the land and ocean contributions along the coastlines. The numerical results from GRACE level 1b data inversion indicate that: (1) MRBF-based gravity modelling reduces the number of parameters by approximately 10%, and allows for more flexible regularization when compared to ordinary RBF solutions; and (2) the resulting MRBF mass flux is shown to better confine the coastal mass variability within the continents. The latter is particularly tested in the Southern Greenland, and our results indicate that the trend of mass loss from the MRBF solution is approximately 11% larger than that from the SH solution, and approximately 4% ~ 6% larger than that from the RBF solution.

1 Introduction of the gravity recovery

Since the launch of Gravity Recovery and Climate Experiment (GRACE) space gravity mission, jointly by NASA and DLR in 2002 with a planned 5-year lifetime [*Tapley et al.*, 2004], GRACE products have been widely used in a number of disciplines to study geophysical processes including earthquake events, melting of ice sheets, as well as oceanic and hydrologic processes [see e.g., *Kusche et al.*, 2012; *Wouters et al.*, 2014]. The majority of these studies relied on the monthly estimates of the Earth's gravity fields, which are publicly available as Level-2 (L2) products released by Center for Space Research at the University of Texas (CSR), NASA's Jet Propulsion Laboratory (JPL), and the German Research Center for Geosciences Potsdam (GFZ), in the form of fully normalized Stokes coefficients [*Bettadpur*, 2012; *Dahle et al.*, 2014; *Watkins and Yuan*, 2012]. However, a significant problem that users of these products face is the presence of correlated and resolution-dependent noise in the Stokes coefficients [*Kusche*, 2007], which manifests itself as "striping" errors in the spatial domain. Therefore, various filtering techniques have to be applied before any geophysical

interpretation can be made, for example: (i) applying post-processing filtering on already computed L2 products; (ii) regularizing the conversion of level-1b (L1b) to L2 products [e.g., *Bruinsma et al.*, 2010; *Save et al.*, 2012].

Designing filters have been extensively addressed in the literature, for instance the implementation of the isotropic filter [*Jekeli*, 1981] or more sophisticated anisotropic filters that decorrelate the Stokes coefficients [e.g., *Swenson and Wahr*, 2006; *Kusche*, 2007]. After filtering, however, mass estimations from GRACE L2 products still contain errors due to the spectral and spatial leakage. The spectral leakage is mainly due to the truncation of the Stokes coefficients (at d/o 60, 90 or 120 in the official products), whereas the spatial leakage is mainly introduced by filtering techniques as most of the available filtering methods contain an averaging kernel that attenuates the magnitude of mass signals accompanied by a possible contamination from neighboring signals. Both classes of leakage errors will lead to a smearing of the actual signals in gravity products because the spatial resolution is not sufficient to capture the processes accurately. In particular, in coastal regions this is a concern as the ocean and land signals are expected to behave very differently, and a signal mixing is undesirable. The state-of-the-art approaches to compensate for signal attenuation due to the spatial leakage mainly comprise post-processing of L2 Stokes coefficients, such as the scale factor method [e.g., *Landerer and Swenson*, 2012; *Long et al.*, 2015] or forward modelling [*Chen et al.*, 2006]. Yet, here we suggest accounting for the leakage correction while inverting L1b data to L2 products. Our work is inspired by *Clarke et al.* [2007], who proposed an application of the sea level equation [see e.g., *Dahlen*, 1976; *Blewitt and Clarke*, 2003] in the SH domain to derive a set of more representative basis functions, which helps to distinguish mass signals distributed over the land and the oceans in the inversion of geodetic site displacement data. This will serve as the foundation for the proposed regional base function approach.

Previous studies addressed the selection of proper basis function as an alternative to the SH approach [see e.g., *Klees et al.*, 2008]. As for instance, the regional geopotential representations by the radial basis functions (RBF) [see e.g., *Schmidt et al.*, 2007; *Eicker*, 2008; *Eicker et al.*, 2013] and mass concentrations (mascon) [see e.g., *Luthcke et al.*, 2006, 2013; *Rowlands et al.*, 2010], have been suggested to be conveniently tailored to the signal characteristics of the specific areas of interest. This feature allows distributing a special type of basis functions along the coastlines, where the spatial leakage is expected to appear, and trying to mitigate it within the GRACE L1b inversion rather than later within the post processing filtering of L2 products. Only recently, *Luthcke et al.* [2013] and *Watkins et al.* [2015] introduced a mass-redistribution step into the mascon parameterization, which aims to more accurately define the coastlines and therefore reduce the spatial leakage. This

step in JPL RL05M mascon model is described as an algorithm to redistribute the mass within a land/ocean mascon (that is placed across coastlines) independently to the land and ocean portions of the particular mascon. This mass redistribution however contains no physical interpretation unlike the implementation of the sea level equation in *Clarke et al.* [2007].

For the first time in this study, we present the parameterization of gravity field recovery using passive-ocean RBFs that are constrained by the sea level equation to account for the spatial leakage. We will particularly show that the application of this method is beneficial along the coastal regions, where considerable spatial leakage smears the actual signals in gravity recovery using the SH or ordinary RBF representation. It is worth mentioning that the RBFs generally comprise two classes: (i) an analytic expression of e.g., point mass as in *Baur and Sneeuw* [2011] and the Abel-Poisson wavelet as in *Schmidt et al.* [2005], and (ii) the so called "band-limited" RBF, which is expressed in a finite spherical harmonic expansion with its spectral behavior generally controlled by a shape kernel such as Shannon, Blackman windows [e.g., *Bentel et al.*, 2013; *Naeimi*, 2013], and harmonic spline functions [*Eicker*, 2008]. Both classes of RBF parameterization have been applied for GRACE L1b inversion [see e.g., *Schmidt et al.*, 2006, 2007; *Wittwer*, 2009; *Gunter et al.*, 2012]. However, prior to this study no attempt has been undertaken to account for the leakage correction during the RBF parameterization.

The proposed passive-ocean RBF is modified from the band-limited RBF class, with the constraint imposed by the sea level equation in three steps: (1) the continental surface mass load is first subtracted from each individual RBF, (2) the passive ocean response to the continental load is then calculated according to the sea level equation, and (3) the continental load and oceanic response are summed to form the modified RBF (MRBF). Our hypothesis is that, the recovered gravity fields via this proposed MRBF allow variability of the load over the continents, and simultaneously impose global mass conservation and equilibrium behavior of the oceans. The contributions of this paper are twofold: (i) mathematically, we show how an ordinary RBF can be modified and constrained by the sea level equation (i.e., here, generating the MRBF), and (ii) an alternative time series of monthly constrained gravity fields in terms of MRBF is now available, and we illustrate that it captures the coastal gravity signals with less spatial leakage compared to the ordinary RBF and SH solutions.

The paper is organized as follows: In Section 2, the theory of RBF modelling and MRBF construction is described. The GRACE L1b processing chain in our in-house gravity field analysis software (called *Hawk*) is outlined in Section 3. Based on this platform, we calculate the monthly gravity products in terms of SH (*Hawk*-SH), RBF (*Hawk*-RBF), and MRBF (*Hawk*-MRBF). In

Section 4, a case study on May 2009 is conducted to illustrate the numerical stability and efficiency of the MRBF. In Section 5, the numerical results for the SH and (M)RBF gravity models are presented. Finally, Section 6 provides a brief summary of the main findings of the study and an outlook of the potential development of the presented MRBF method.

2 Methods

2.1 Radial basis function modelling

The most general form of a band−limited RBF $\Phi_i(\Omega_i, \Omega)$, located at the geographic position Ω_i on the sphere, is defined as a finite SH series [*Eicker*, 2008] as

$$\Phi_i(\Omega_i, \Omega) = \frac{GM}{R} \sum_{n=2}^{N_{max}} (\frac{R}{r})^{n+1} \phi_n \sum_{m=-n}^{n} Y_{nm}(\Omega_i) Y_{nm}(\Omega) \quad , \tag{1}$$

where Ω is the geographic position of an arbitrary point, r is the distance from the geocenter, GM is the Earth constant parameter, R is the mean radius of the Earth, and Y_{nm} is the SH of truncation degree n and order m. In particular, the shape coefficients ϕ_n that define the shape of the RBF, and the truncated degree N_{max} that relates to the bandwidth of RBF, are the most critical factors to determine the spectral behavior of the RBF. To date, there are various RBFs in use for gravity recovery, of which the simplest is defined by the Shannon kernel [*Keller*, 2004]:

$$\phi_n = \begin{cases} 1 & n \in [2, N_{max}] \\ 0 & n, elsewhere \end{cases} \tag{2}$$

This Shannon kernel with $N_{max} = 90$ is also employed in our study to construct the RBF, since it does not impose additional smoothness constraints in the spectral domain. Subsequently, we model the gravity field $V(\Omega)$ using this set of RBFs distributed on the sphere, as follows:

$$V(\Omega) = \sum_{i=1}^{I_{max}} a_i \Phi_i(\Omega_i, \Omega) \quad , \tag{3}$$

with those scaling parameters a_i found by least-squares adjustment from GRACE L1b observations. In particular, the parameter I_{max} defines the number of RBFs distributed on the Earth surface in a given network geometry. Since the icosahedral gridding [*Sadourny et al.*, 1968] in the level of $I_{max} = 9002$ enables a relatively uniform and sufficiently dense coverage on the sphere, it is chosen to construct our RBF gridding network.

2.2 Developing the modified radial basis function(MRBF)

RBFs are entirely isotropic, according to their definition (Eq. (1)). Yet, ocean mass represented by isotropic RBFs does not account for the passive ocean response [e.g., *Dahlen*, 1976] that land load causes and that has a significant effect along coastlines. Our hypothesis is that by developing an anisotropic MRBF that accurately models this response we will be able to separate land and ocean mass signals and more adequately reduce possible leakage.

It should be kept in mind that the RBF by Eq. (1) describes potential changes, while adding the underlying spatial constraint has to be applied at the level of the surface mass distribution. Therefore, each potential function RBF $\Phi_i(\Omega_i, \Omega)$ is transformed first to the function of EWH (Equivalent-Water Height) by $\Psi_i(\Omega_i, \Omega)$ that represents the surface mass [e.g., *Wahr et al.*, 1998] as follows,

$$\Psi_i(\Omega_i, \Omega) = \sum_{n=2}^{N_{max}} \frac{R\rho_e}{3\rho_s} \frac{2n+1}{1+k_n} \phi_n \sum_{m=-n}^{n} Y_{nm}(\Omega_i) Y_{nm}(\Omega) \quad , \tag{4}$$

where ρ_e denotes the average Earth density, ρ_s denotes the sea water density and k_n is the elastic load Love number (LLN) for degree n. The LLNs from *Wang et al.* [2012] are used in this study.

One can observe from Eq. (4) that, any physical constraint added to $Y_{nm}(\Omega)$ will ultimately transfer to $\Psi_i(\Omega_i, \Omega)$ via a linear transformation. This finding suggests a directly modifying $Y_{nm}(\Omega)$ rather than $\Psi_i(\Omega_i, \Omega)$, since $Y_{nm}(\Omega)$ is free of the quantity Ω_i that varies with the gridding type. Consequently, before the $\Psi_i(\Omega_i, \Omega)$ being investigated, we first need to introduce constraint of the sea level equation into $Y_{nm}(\Omega)$, to creat a new set of functions $B_{nm}(\Omega)$ that consistently and accurately represent the surface mass load. Here, we follow the approach proposed by *Clarke et al.* [2007] to derive them.

In the first step, we form an initial basis $B'_{nm}(\Omega)$ (representing the continental load) by applying the ocean mask $C(\Omega)$, a function defined to be zero over the continents and unity over the oceans, to the spherical harmonic $Y_{nm}(\Omega)$, following

$$B'_{nm}(\Omega) = (1 - C(\Omega)) \cdot Y_{nm}(\Omega) \approx \sum_{j=0}^{N_{max}} \sum_{k=-j}^{j} b'_{nm,jk} Y_{jk}(\Omega) \quad . \tag{5}$$

The coefficients $b'_{nm,jk}$ are derived from the product-to-sum operator that comes from the Wigner$-3j$ symbol [*Rasch and Yu*, 2004] in combination with the SH expansion coefficients of the ocean function. As pointed out by [*Blewitt et al.*, 2005; *Clarke et al.*, 2007], the evaluation of $b'_{nm,jk}$ up to degree and order 90 ($N_{max} = 90$) requires the availability of the ocean coefficients up to twice the N_{max} (i.e. 180). Otherwise, an omission error likely appears.

In addition to the continental (dynamic) load $B'_{nm}(\Omega)$, the total time-variable load exerted on the Earth also comprises the oceanic response, introducing a passive oceanic load $S_{nm}(\Omega)$. This term follows the 'sea level equation', prescribing that the oceanic passive load is in hydrostatic equilibrium with the gravitational potential field due to the total (dynamic plus passive) load [*Clarke et al.*, 2005]. This mathematically enforces that (i) the degree-zero terms of $S_{nm}(\Omega)$ and $B'_{nm}(\Omega)$ cancel out so that total mass load is conserved, and (ii) the remaining harmonic coefficients of $S_{nm}(\Omega)$ yield to the input load $B'_{nm}(\Omega)$ in the form of

$$S_{nm}(\Omega) = \xi(B'_{nm}(\Omega)) = \sum_{j=0}^{N_{max}} \sum_{k=-j}^{j} s_{nm,jk} Y_{jk}(\Omega) \quad , \tag{6}$$

where ξ represents the operator that solves the sea level equation in the spectral domain, and the $s_{nm,jk}$ are the Stokes coefficients that should be estimated. Further details on the sea level equation and its solution can be found in e.g. *Dahlen* [1976], *Spada and Stocchi* [2007] as well as the provided electronic supporting material.

In the final step, we correct the $B'_{nm}(\Omega)$ by adding the passive oceanic load $S_{nm}(\Omega)$, and form the "self-consistent" base $B_{nm}(\Omega)$, which therefore enforces global mass conservation and simultaneously separates ocean signals from land load. With a summation of Eq. (5) and Eq. (6), $B_{nm}(\Omega)$ is represented in an expansion of SHs, given by

$$B_{nm}(\Omega) = B'_{nm}(\Omega) + S_{nm}(\Omega) = \sum_{j=1}^{N_{max}} \sum_{k=-j}^{j} b_{nm,jk} Y_{jk}(\Omega) \quad ,$$

$$b_{nm,jk} = b'_{nm,jk} + s_{nm,jk} \quad . \tag{7}$$

As shown here by a number of examples $(Y_{4,0}, B_{4,0}, S_{4,0})$, $(Y_{4,3}, B_{4,3}, S_{4,3})$ in Fig. 1, the physical constraints built inside the B_{nm} do take effect and successfully distinguish between the land and ocean. Nevertheless, our ultimate objective is to transform the constraints into the radial basis functions. Having $B_{nm}(\Omega)$ from Eq. (7), we replace them in Eq. (4), which yields

$$\Psi_i^{new}(\Omega_i, \Omega) = \sum_{n=2}^{N_{max}} \frac{R\rho_e}{3\rho_s} \frac{2n+1}{1+k_n} \phi_n \sum_{m=-n}^{n} Y_{nm}(\Omega_i) B_{nm}(\Omega)$$

$$= \sum_{j=1}^{N_{max}} \sum_{k=-j}^{j} \{ \sum_{n=2}^{N_{max}} \sum_{m=-n}^{n} \frac{R\rho_e}{3\rho_s} \frac{2n+1}{1+k_n} \phi_n Y_{nm}(\Omega_i) b_{nm,jk} \} Y_{jk}(\Omega) \quad . \tag{8}$$

In this manner, the revised surface mass distribution $\Psi_i^{new}(\Omega_i, \Omega)$ automatically inherits the physical constraint within $B_{nm}(\Omega)$, so that $\Psi_i^{new}(\Omega_i, \Omega)$ is self-consistent as well. Furthermore, the modified radial basis function (MRBF), shown by $\Phi_i^{new}(\Omega_i, \Omega)$, can be obtained by converting the
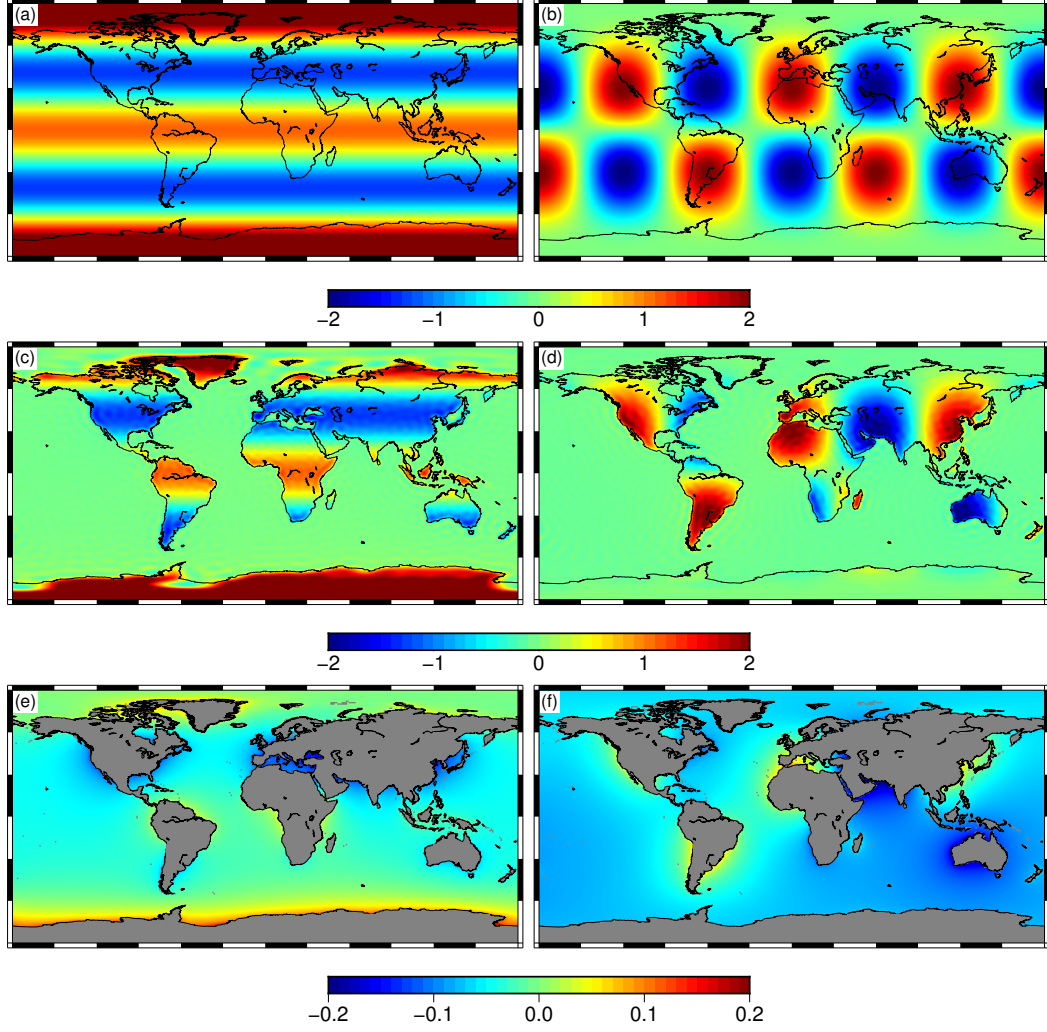
Figure 1. Spherical harmonics Y_{nm} and the respective self-consistent bases B_{nm} as well as the passive ocean response S_{nm}: (a)(c)(e) are $Y_{4,0}$, $B_{4,0}$, $S_{4,0}$, respectively; and (b)(d)(f) are $Y_{4,3}$, $B_{4,3}$, $S_{4,3}$, respectively.

surface mass distribution $\Psi_i^{new}(\Omega_i, \Omega)$ into a potential function, such that

$$
\begin{aligned}
\Phi_i^{new}(\Omega_i, \Omega) &= \frac{GM}{R} \sum_{j=1}^{N_{max}} \left(\frac{R}{r}\right)^{j+1} \frac{\rho_s}{R\rho_e} \frac{1+k_j}{2j+1} \sum_{k=-j}^{j} \left(\sum_{n=2}^{N_{max}} \sum_{m=-n}^{n} \frac{R\rho_e}{3\rho_s} \frac{2n+1}{1+k_n} \phi_n Y_{nm}(\Omega_i) b_{nm,jk} \right) Y_{jk}(\Omega) \\
&= \frac{GM}{R} \sum_{j=1}^{N_{max}} \left(\frac{R}{r}\right)^{j+1} \sum_{k=-j}^{j} \left(\sum_{n=2}^{N_{max}} \sum_{m=-n}^{n} \frac{1+k_j}{2j+1} \frac{2n+1}{1+k_n} \phi_n Y_{nm}(\Omega_i) b_{nm,jk} \right) Y_{jk}(\Omega) \quad ,
\end{aligned}
\tag{9}
$$

from which the summation is found to begin from degree-one ($j = 1$) rather than from degree-two. Therefore, the degree-one terms are added in our inversion as well. But on the other hand, as current

–8–

GRACE mission is not sensitive to the degree-one potential, one would not be able to derive a meaningful degree-one harmonic from the MRBF coefficients by transformation. By substituting Eq. (9) into Eq. (3), the ultimate gravity field represented by MRBFs is derived.

As of now, the method of constructing MRBF has been fully established. In what follows, we give an insight into the nature of the proposed MRBF. Unlike the RBFs that have the same shape, we realize from Eq. (9) that each individual MRBF is unique and its shape varies with the location Ω_i. To this end, we exemplarily investigate the four scenarios in Fig. 2, which display how the (M)RBF bases will perform if they are near or far from the coastline. One can see from Fig. 2 that, (i) the MRBF and RBF over the interior land are fairly similar (Fig. 2 top-right versus top-left), indicating this MRBF maintains the property of mass-concentration; (ii) however, the oceanic signals of the MRBF along the coastline has been considerably attenuated as expected, compared to that of the RBF along the coastline (Fig. 2 bottom-right versus bottom-left). Nevertheless, it has to be made clear that the spatial leakage of MRBF (signals over the ocean) cannot be completely reduced because MRBFs are still represented by a band-limited harmonic expansion (N_{max} = 90).

Additionally, we note that our MRBF solution does not indicate a global distribution of MRBF bases, but a scheme of combining ordinary RBFs over the ocean (ocean-RBFs) with MRBFs over the land (land-MRBFs) together. Our reasoning is: (i) the ocean-RBFs rather than the ocean-MRBFs can remain the property of mass-concentration, so that the orthogonality of the bases can be guaranteed. (ii) The actual ocean variability generally consists of three contributions: ocean-land mass exchange, equilibrium ocean response to the land load, and non-equilibrium ocean dynamic variability. The former two components have been inherently considered by the land-MRBFs, while modelling the latter one component is only feasible by the ocean-RBFs rather than ocean-MRBFs. (iii) In principle, land-MRBFs have only considered the first class of spatial leakage from land to ocean, whereas use of the ocean-RBFs does not account for the second class of leakage from ocean to land; however, the amplitudes are less over the oceans [see, *Clarke et al.*, 2007].

3 The GRACE L1b data processing chain

Hawk, our in-house software for the analysis of gravity recovery from GRACE observations, comprises code implementations of all procedures described and applied within this study. Based on *Hawk* and release 02 GRACE L1b raw data [*Case et al.*, 2002], all generated gravity fields presented here share the same data processing chain.
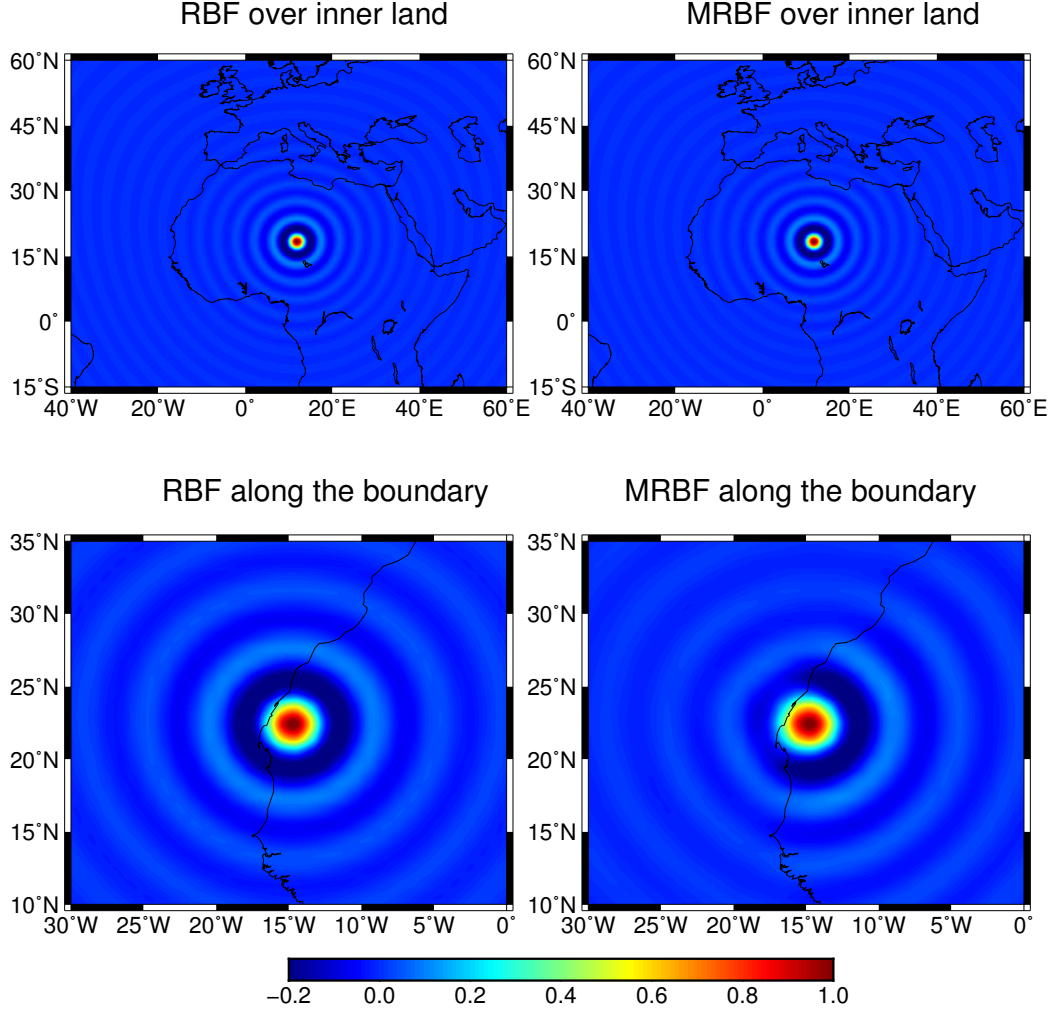
Figure 2. EWHs derived from RBF (left) that consists of Y_{nm}, as well as from MRBF (right) that consists of B_{nm}. Two types of locations (near the coastline, and over the inner land far away from the coastline) are investigated.

3.1 Reference systems, background models and data

The reference systems we rely on consist of (i) an inertial coordinate system within IERS (International Earth Rotation Service) celestial reference frame, and (ii) an Earth-fixed coordinate system consistent with the ITRF2008 (International Terrestrial Reference Frame 2008) convention. The EOP (Earth Orientation Parameters) are obtained from the public IERS file EOP-08-C04.

244   **Table 1.**   Summary of background models implemented in the *Hawk* software

Force Model	Source	Resolution
Mean gravity field	GIF48	Degree/order 160
Solid tide	IERS2010 non-elastic Earth	Degree 2,3 and 4[a]
Ocean tide	EOT11a	Degree/order 120
Solid pole tide	IERS2010 non-elastic Earth	
Ocean pole tide	IERS2010 convention	Degree/order 30
Non-tidal atmosphere and ocean de-aliasing	AOD1B RL05	Degree/order 100
Third-body perturbations	JPL DE405	Sun and Moon only[b]
General relativity	IERS2010 convention	Sun and Earth
Non-conservative forces	ACC1B and SCA1B	GRACE L1b product

[a] it contains 234 secondary tides.   [b] J2 indirect effect is also considered.

231   Additionally, JPL DE405 planetary ephemeris [*Standish*, 1995] is adopted to approximate trajectories

232   of Sun and Moon.

233   Background models employed within our work are briefly summarized in Table 1. The nominal

234   mean gravity field is modeled by GIF48 [*Ries et al.*, 2011] complete up to d/o 160, which is sufficient in

235   practice to recover monthly gravity signals up to d/o 60 or 90. Subsequently, third-body gravitational

236   perturbations, together with the indirect J2 effect, are computed from the positions and velocities of

237   Sun and Moon only. Effects of ocean tides are removed via EOT11a model [see, e.g., *Savcenko*

238   *and Bosch*, 2012], which is up to d/o 120 and comprises 18 major waves (eight long periodic, four

239   diurnal, five semidiurnal, one nonlinear waves) and 238 secondary waves. Furthermore, the short

240   period nontidal variability in the atmosphere and oceans are removed using the official AOD1B RL05

241   de-aliasing product [*Flechtner et al.*, 2013]. The remaining gravitational forces including solid Earth

242   (and pole) tides, ocean pole tides, as well as general relativistic perturbations are modeled according

243   to the International Earth Rotation Service (IERS) 2010 conventions [*Petit and Luzum*, 2010].

245   K-band range rate (KBRR) measurements [*Kim*, 2000], along with GPS pseudo-range and

246   phase measurements, are in general the primary observations processed in official GRACE L2

247   products. However, in our analysis scheme, the kinematic orbits published by ITSG (Institute

248   of Theoretical Geodesy and Satellite Geodesy) at Graz University of Technology (`ftp://ftp.`

254

Table 2. Summary of GRACE measurements used in *Hawk* software

Observations	Version	Sampling rate
Kinematic orbit	ITSG	Uneven, mostly 10s
K-band range-rate	GRACE L1b RL02	5s

249 `tugraz.at/outgoing/ITSG/tvgogo/orbits/`), along with the L1b KBRR measurements, serve

250 as the observations instead. It is known that the main contribution to GRACE gravity recovery comes

251 from the KBRR measurements because of its high accuracy, hence the random error introduced by

252 kinematic orbits will not significantly bias the solution. An overview of the measurements used in

253 this study is given in Table 2.

255 **3.2 Parameterization**

256 The theoretical method we adopt to set up observation equations follows the classical variational-

257 equation approach, which is employed by CSR, GFZ and JPL in their official GRACE L2 analysis

258 schemes as well. However the length of orbital arcs is selected as 3 hours in our work, which differs

259 from the strategy of other institutes.

260 For each 3 hour arc, the partial derivatives for Stokes coefficients (or (M)RBF scaling factors),

261 accelerometer instrument biases and drifts along 3-axes [*Bettadpur*, 2009], GRACE twin-spacecraft

262 initial state vectors, and KBRR nuisance parameters [*Kim*, 2000] (for more details, see Table 3)

263 are derived. With these partial derivatives, the observation equations are set up for the KBRR

264 observations and kinematic orbit pseudo-observations separately. Subsequently, these two types of

265 equations are combined in terms of a constant weight determined by the nominal accuracy information

266 of kinematic orbit and KBRR, which are regarded as 1~2 cm and 0.1~0.2 um/s [*Kang et al.*, 2009;

267 *Beutler et al.*, 2010].

269 After eliminating the arc-specific parameters, we form the individual normal equations arc by

270 arc. The arc-specific parameters in this study generally comprise the accelerometer biases and drifts,

271 the initial state vectors and the KBRR biases. With these procedures, the final normal equations are

272 accumulated for one month and solved for the global geopotential parameters, such as the Stokes

273 coefficients or (M)RBF parameters.

268   **Table 3.**   Summary of estimated parameters in the *Hawk* software

Parameter	Physical quantities	Number of estimate	Time sampling
Twin Satellite state	Position and velocity	12	3 hourly
Accelerometer bias	X,Y,Z components	6	3 hourly
Accelerometer drift	X,Y,Z components	6	3 hourly
KBR range-rate biases	Constant, drift, one CPR	4	3 hourly
Stokes coefficients	90×90 or 60×60	8366 or 3776	Monthly
or (M)RBF scaling	Level 30 icosahedral	9002	Monthly
factors	gridding[a]		

[a] The number of estimate I_{max} for icosahedral gridding relates to the level i as $I_{max} = 10 \cdot i^2 + 2$.

3.3 Validation via real GRACE L1b data inversion

275   To enable an objective assessment of (M)RBF approach, we have to isolate the parameterization-

276   specific effects. To this end, a validation of the parameterization is essential. A time series of

277   unconstrained monthly gravity fields in terms of spherical harmonic up to d/o 60, called *Hawk*-SH60,

278   is produced and compared to the state-of-the-art SH-based gravity models that are publicly available

279   at International Center for Global Earth Model (ICGEM `http://icgem.gfz-potsdam.de`).

282   In what follows, we calculate the mean of 6-years (from January 2005 to December 2010)

283   gravity fields for CSR RL05, GFZ RL05a and JPL RL05 as well as *Hawk*-SH60, respectively.

284   Figure 3 illustrates the spectrum of geoid heights versus degree derived from the respective mean

285   model. Evidently, *Hawk*-SH60 agrees well with the official products at all spectral components. In

286   particular, the correlation coefficient between *Hawk*-SH60 and CSR RL05 is as high as 0.99, whereas

287   it only amounts to 0.89 between GFZ RL05a (up to d/o 90) and CSR RL05 (up to d/o 60). Reasons

288   for the high correlation coefficient between our model and CSR RL05 are the use of the similar

289   background models and the same truncation at d/o 60. In addition to the comparison of per-degree

290   geoid heights, further validation results can be found in the provided electronic supporting material.

291   Above result illustrates that our parameterization is well suited for accurate GRACE L1b inversion.

292   In this context, any progress of (M)RBF-based gravity fields shown in the following will be always

293   ascribed to the evolution of the geopotential representation itself, or more specifically, the embedded
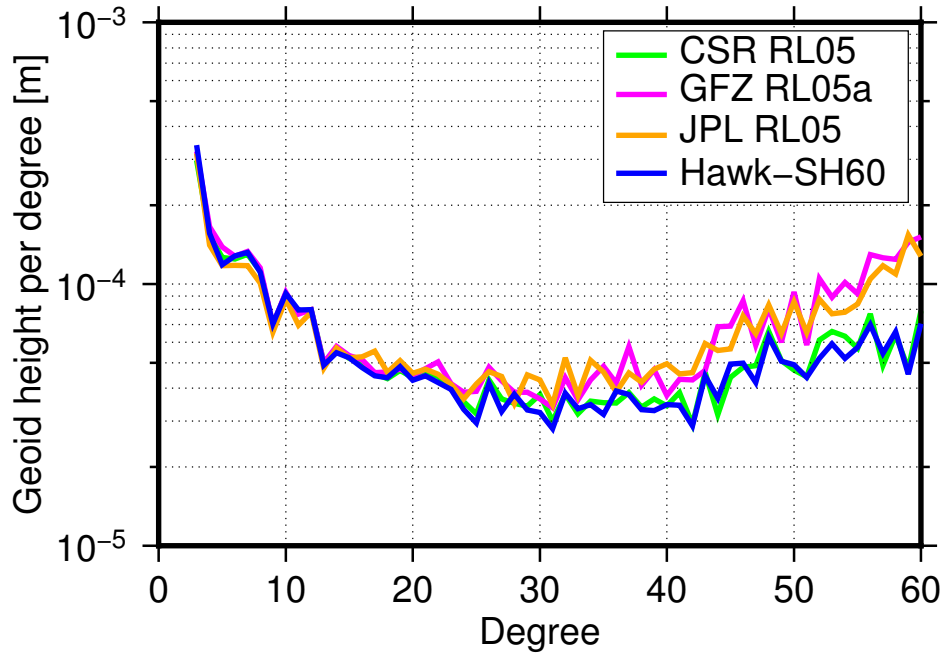
294   physical constraints.

Figure 3. Geoid heights per degree are derived from the mean (2005~2010) for CSR RL05, GFZ RL05a, JPL RL05 and *Hawk*-SH60 monthly gravity fields, with respect to GIF48.

4 The efficiency and stability of MRBF: case study on May 2009

4.1 Test of the numerical efficiency for unconstrained solutions

In our experiments, the numerical efficiency of the inversion strongly depends on the number of unknowns, such as the Stokes coefficients for SH solution or gridding nodes for (M)RBF solutions. In this context, we intend to evaluate the RBF and MRBF unconstrained solutions with the minimum number of gridding nodes that is required to accurately model the gravity fields.

One assumption in our study is that, by increasing the gridding nodes, the unconstrained (M)RBF solutions will eventually get approximate to the unconstrained SH-based model like GFZ RL05a. Otherwise, too sparse gridding distribution will fail the solution. The departure of this assumption is the concept addressed by previously published results that, a simple base change from SH to RBF or mascon does not inherently provide an advantage in obtaining a more accurate global unconstrained gravity field. As for example, *Wittwer* [2009] demonstrated that the RBF-based solution (fundamentally different with our RBF parameterization) is fairly similar to the SH solution

particularly up to d/o 30; *Rowlands et al.* [2010] and *Watkins et al.* [2015] illustrated that their
unconstrained mascon solutions are equivalent to the state-of-the-art SH solutions up to d/o 60.

In support of our assumption, several scenarios of the unconstrained MRBF versus unconstrained
SH models are shown in Fig. 4a. Firstly, the results again illustrate that our data processing chain
is reliable, as evidenced by the fact that the correlation coefficient between GFZ RL05a curve (the
red solid line) and *Hawk*-SH90 curve (the green solid line) is as large as 0.96, and the correlation
coefficient between *Hawk*-SH60 curve (the purple solid line) and CSR RL05 curve(the blue solid
line) is 0.99. More importantly, we find from Fig. 4a that, the unconstrained MRBF solution and
SH solution indicate almost the same amount of power, for instance, the gray dashed line versus the
purple solid line (correlation coefficient is ∼1.00), and the orange dashed line versus the green solid
line (correlation coefficient is ∼1.00). This finding is consistent with the previously published results
[e.g., *Rowlands et al.*, 2010], and it shall serve as the foundation for assessing the efficiency of the
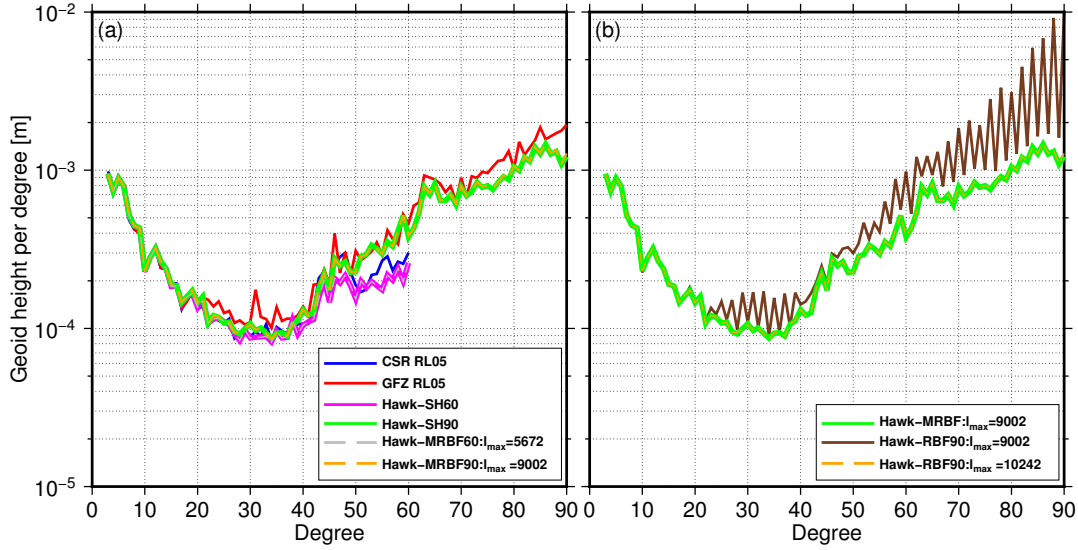(M)RBF approaches.

Figure 4. Illustration of per-degree geoid heights [m] on May 2009 for various models, where *Hawk*-SH60
stands for our SH models up to degree 60, *Hawk*-MRBF60 denotes the MRBF model with shape coefficients
up to $N_{max} = 60$, and so on. **(a)** SH solutions versus the MRBF solutions associated with various schemes; **(b)**
MRBF solution in a gridding level $I_{max} = 9002$ versus RBF solutions in gridding levels $I_{max} = [9002, 10242]$.

In this context, the unconstrained gravity fields in terms of RBFs and MRBFs are expected to
have roughly the same degrees of freedom (I_{max}). Regarding that the network geometry $I_{max} = 9002$

has enabled an accurate MRBF modelling (shown in Fig. 4a), we will mainly investigate how it

performs in the RBF solution. The *Hawk*-RBF90's per-degree geoid height (denoted by the gray

line) is displayed in Fig. 4b, from which we however find an unexpected oscillation occurring after

degree 20. The gridding scheme $I_{max} = 9002$, which might be not sufficiently dense for the accurate

RBF modelling, is assumed to be responsible for the oscillation. In support of our conjecture, we

carry out an alternative RBF solution associated with $I_{max} = 10242$ that is slightly larger than the

previous, and for this time the oscillation vanishes and the *Hawk*-RBF90 ultimately converges to the

Hawk-MRBF90 (see Fig. 4b, the green solid line and the orange dashed line overlap closely). As a

summary, the minimal required I_{max} for RBF is 10242, while for MRBF the minimal required I_{max}

is 9002. This reveals that the inherent physical constraints within MRBF are favorable for lowering

the rigid requirement of gridding nodes ($\sim 10\%$), as well as increasing the numerical efficiency

rapidly.

4.2 Test of the numerical stability via a Tikhonov regularization

Compared to the SH solution, the added value of (M)RBF approaches is their convenience to

implementing tailored regularization at areas of interest, as (M)RBFs are more regionally specified.

In general, GRACE L1b inversion is a typical ill-posed problem coupled with the necessity of

regularization to stabilize the solution, given by [*Tapley et al.*, 2004]

$$(H^T W H + \lambda N)\hat{x} = H^T W y + \lambda N \bar{x} \quad . \tag{10}$$

In Eq. (10), H is a matrix of partial derivatives of the GRACE observations y, given in Table 2,

with respect to vector of the estimated parameters $\hat{x}$, list in Table 3; W is a weighting matrix for the

observations, $\bar{x}$ are a-priori values of the estimated parameters $\hat{x}$, N represents the regularization

matrix that contains a priori covariance information of the estimated parameters, λ is introduced as

the regularization parameter to tune the strength of regularization and the optimal λ can be found by

various methods [see, e.g., *Koch and Kusche*, 2002; *Kusche and Klees*, 2002; *Save*, 2009]. According

to Eq. (10), the components N, $\bar{x}$ have to be predefined in a proper way. Among various regularization

methods, Tikhonov regularization [*Tikhonov and Arsenin*, 1977] is perhaps the simplest and most

commonly used one so far. In this study, Tikhonov regularization is specified by setting $\bar{x} = 0$, and

354   N as a diagonal matrix with its diagonal elements designed with σ_i, that is

355
$$N = \begin{bmatrix} 1/\sigma_1^2 & 0 & 0 & 0 \\ 0 & 1/\sigma_2^2 & 0 & 0 \\ \vdots & \vdots & \vdots & \vdots \\ 0 & 0 & 0 & 1/\sigma_{I_{max}}^2 \end{bmatrix} , \qquad (11)$$

356   where σ_i denotes the standard deviation of the signals. Regarding to the construction of the

357   regularization matrix N, we adopt a regionally adapted method according to *Eicker* [2008] that: σ_i

358   of the (M)RBF is assigned with a relative value that, to some extent, infers the a priori feature of

359   the geophysical signals over the areas where the (M)RBF is located. To this end, we classify the

360   (M)RBF gridding into the ocean and land areas, which yields

361
$$\sigma_i^2 = \begin{cases} 1 & i \in land \\ 1/\Sigma & i \in ocean \end{cases} . \qquad (12)$$

362   In the majority of cases, a valid assumption is that, the geophysical signals over the oceans are

363   far less rough than that over the continents. Therefore, the standard deviation σ_i of oceanic signals

364   is supposed to be relatively small ($\Sigma > 1$) in Eq. (12). To this end, we conduct several scenarios by

365   varying the ocean smoothness factor $\Sigma = [1, 2, 5, 10, 20]$ within the regularization matrix N for RBF

366   and MRBF solutions, respectively.

372   Figure 5 illustrates the resulting (M)RBF-based gravity fields in terms of EWH for May 2009. In

373   particular, we zoom in to the region of South America in Fig. 5 for a better comparison. Considering

374   the case of RBF (see Fig. 5 , the six plots on top), it can be observed from the right side of Fig.

375   5(a) that, a striping error still exists over the ocean even after regularization $\Sigma = 1$. While as soon

376   as $\Sigma = 1$ increases (from Fig. 5(a) to Fig. 5(e)), the striping error is getting smaller, revealing that

377   the ocean smoothness factor does take effect as expected. However, continental variability is getting

378   unstable and is rapidly deteriorating when Σ increases, since the signals are getting more and more

379   point-shaped from Fig. 5(a) to Fig. 5(e), which are not expected. To demonstrate the instability,

380   the differences of continental variability between Fig. 5(a) and Fig. 5(e) are given at Fig. 5(f), and

381   the statistic over the South America is $min/max/wRMS = -917/1212/117 [mm]$, which is strong

382   enough to affect realistic mass estimation. On the contrary, for MRBF solution (see Fig. 5, the six

383   plots on bottom), no evident differences of the continental mass variability can be distinguished from

384   Fig. 5(g) to Fig. 5(k). The statistic of Fig. 5(l) is $min/max/wRMS = -323/434/23 [mm]$, which

385   is much smaller than that of Fig. 5(f). Simultaneously, we find the oceanic striping noise is getting

386   smoothed as soon as Σ increases as well (see from Fig. 5(g) to Fig. 5(k)).
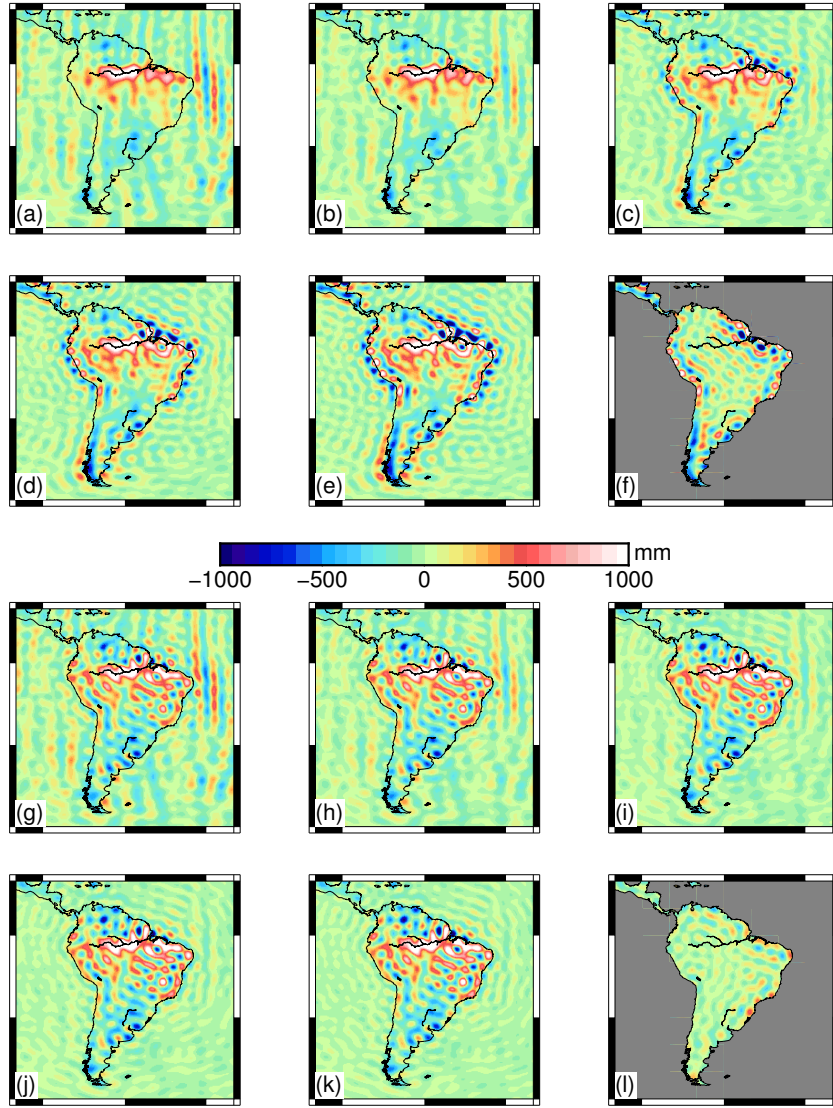
Figure 5. Mass anomaly in terms of EWH, derived from RBF (top six) and MRBF (bottom six) solutions associated with different regularization scheme for May 2009: (a)(b)(c)(d)(e) are the RBF solutions with $\Sigma = 1, 2, 5, 10, 20$, respectively; (f) presents the differences between (e) and (a) with ocean mask; (g)(h)(i)(j)(k) are the MRBF solutions with $\Sigma = 1, 2, 5, 10, 20$, respectively; (l) presents the differences between (k) and (g) with ocean mask.

We suppose the spurious point-shaped continental variability in regularized RBF solutions are introduced by the mixing between oceanic and continental signals while smoothing the ocean noise ($\Sigma = [1, 2, 5, 10, 20]$). However, the physical constraint that is satisfied by the MRBFs ensures an

efficient separation of ocean and land signals across the coastlines. As a result, this yields a more robust continental mass estimate that is less subjective to the ocean smoothing.

To confirm our hypothesis, we further assess the spectral behavior of the regularized RBF and MRBF solution on May 2009. The per-degree geoid heights of standard (Σ=1) Tikhonov regularized (M)RBF and unconstrained SH solutions are illustrated in Fig. 6, from which it is evident that both RBF and MRBF have shown an overall agreement prior to d/o 60. Although they both show suppressed signals and errors in the higher degree spectrum, there are still considerable differences after d/o 60, which indicate that the MRBF solution may improve the short-wave gravity signals. In what follows we further vary the regularization schemes ($\Sigma = [1, 2, 5, 10, 20]$) in Fig. 7, from which we find the MRBF curves are gradually converging to a stable status when Σ increases; however, the RBF curves are gradually getting unstable and divergent, particularly at around degree 30 and further degrees that mainly infer the medium-wavelength gravity signals. Additionally, the stronger ocean smoothing by $\Sigma > 2$ has artificially led to a comeback of the high-degree error after d/o 60 (see Fig. 7(a), the end of cyan curve lies much higher than the red curve), which were shown in Fig. 5(a-e) as the point-shaped perturbation. This experiment demonstrates that the regularization of RBF solution has to be treated very carefully, while MRBF is robust to regularization in the sense of a flexible ocean smoothing without increasing instability.

However, one can observe from the above experiments that, the side effects such as the spurious continental noise brought by the regularization into MRBF and RBF gravity fields are unequal. Therefore, to enable a fair comparison between RBF and MRBF solutions, both of these two solutions in the following section shall be conditioned by the standard Tikhonov regularization ($\Sigma = 1$) that we believe to have the least inequity (see Fig. 6).

5 MRBF versus RBF and SH monthly solutions for 2005-2010

In general, the regularized gravity field from GRACE does not require to be spatially filtered as this has been often considered in the regularization. Yet, in this study, the simple standard Tikhonov regularization was found not to be sufficient to suppress the striping errors (see Fig. 5, the magnitude of the noise is still non-negligible for both RBF and MRBF solutions). Therefore, another Gaussian filtering with a radius of 200km has been applied to the regularized (M)RBF solutions for all the following applications, unless otherwise mentioned. In this way, the global mass anomaly in terms of EWH on January, May and September are exemplarily shown in Fig. 8 from the top to the bottom. And from the left panels to the right panels in Fig. 8 are the EWH maps of RBF solutions,
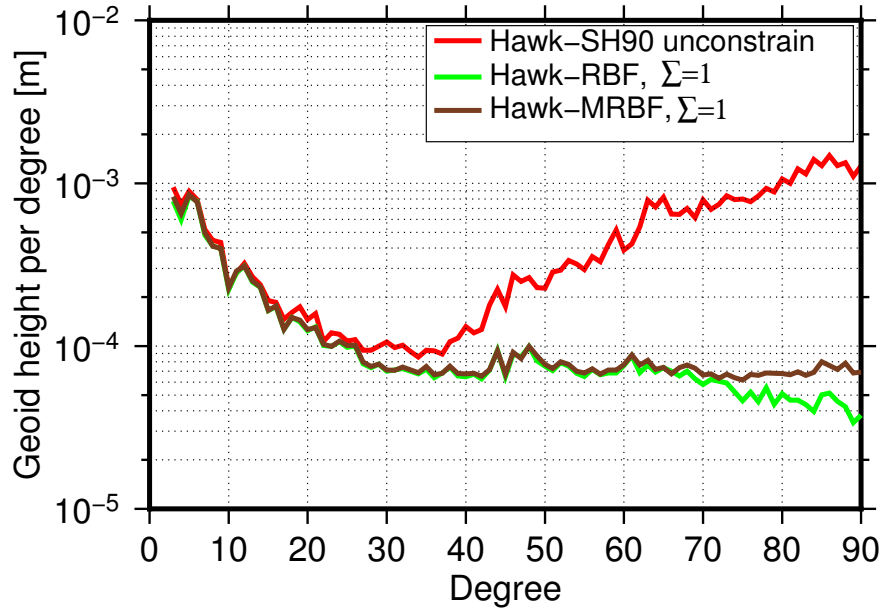
Figure 6. Illustration of per-degree geoid height derived from following models: unconstrained SH solution *Hawk*-SH90, constrained RBF solution *Hawk*-RBF90 with a standard Tikhonov regularization ($\Sigma = 1$), and MRBF solution *Hawk*-MRBF90 with a standard Tikhonov regularization ($\Sigma = 1$).
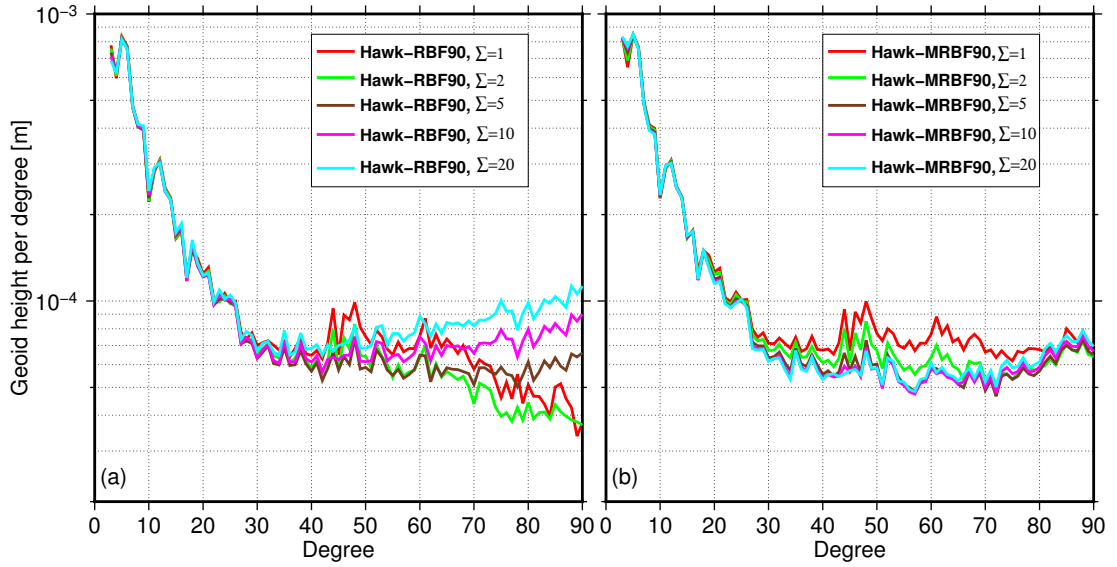

Figure 7. **Left** are per-degree geoid heights derived from RBF solutions with $\Sigma = 1, 2, 5, 10, 20$, respectively; **Right** are per-degree geoid heights derived from MRBF solutions with $\Sigma = 1, 2, 5, 10, 20$, respectively.

438   **Table 4.**   Statistics for RBF and MRBF solutions in Fig. 8

Month	*Hawk*-RBF[a] [mm]	*Hawk*-MRBF [mm]	Correlation coefficients[b]
Jan 2010	Fig. 8(a): -714/194/53	Fig. 8(b): -685/204/49	0.92
May 2010	Fig. 8(d): -708/308/55	Fig. 8(e): -713/296/51	0.93
Sep 2010	Fig. 8(g): -777/293/71	Fig. 8(h): -733/320/66	0.92

[a] Statistics for spatial EWH: min/max/weighted RMS.

[b] In terms of the curves of the per-degree geoid height before d/o 30.

426   MRBF solutions and their differences, respectively. The statistic for Fig. 8 is given in the Table

427   4, from which we find that both of the spatial EWH and the correlation coefficients show a general

428   agreement between the RBF and MRBF solutions, hinting that in large basins (or medium-to-long

429   wavelength gravity field) both solutions perform well. We note that, in Table 4, the weighted RMS

430   of MRBF solution is usually less than that of RBF solution because the MRBF reduces the oceanic

431   signals. Furthermore, as illustrated by the maps of differences in Fig. 8(c)(f)(i), discrepancies

432   between the RBF and MRBF solution exist mostly at coastal areas, such as the coast of Greenland

433   and Antarctica that have the most significant spatial leakage in ordinary solutions. Considering the

434   case of September 2010 (see Fig. 8(i)), the weighted RMS of oceanic signals within the region of

435   Greenland ($[5°W, 85°W], [58°N, 85°N]$) is $87mm$ for *Hawk*-RBF, and $34mm$ for *Hawk*-MRBF. This

436   finding indicates a possible reduction of ocean leakage as well as the improvement of the resolution

437   at coastal areas for the MRBF solutions.

443   In what follows we particularly investigate the seasonal and secular mass flux signals for gravity

444   solutions of different types. The comparisons of GFZ RL05a, *Hawk*-SH, *Hawk*-RBF and *Hawk*-

445   MRBF are carried out, but we note that, because these models are computed from GRACE-only

446   observations, this is indeed not an external validation experiment. It should be also pointed out

447   that the Gaussian filter with a radius of 500km is applied to the unconstrained SH solutions (*Hawk*-

448   SH and GFZ RL05a). The radius of 500km is selected because in this way the noises are found

449   suitably damped in the SH-based solutions, and the noise level of these filtered SH-based solutions

450   are comparable to that of the regularized (M)RBF solutions. As for example, the RMS (root mean

451   square) value of the basin-averaged mass variation over Sahara desert ($[21°S, 5°N], [45°W, 80°W]$)

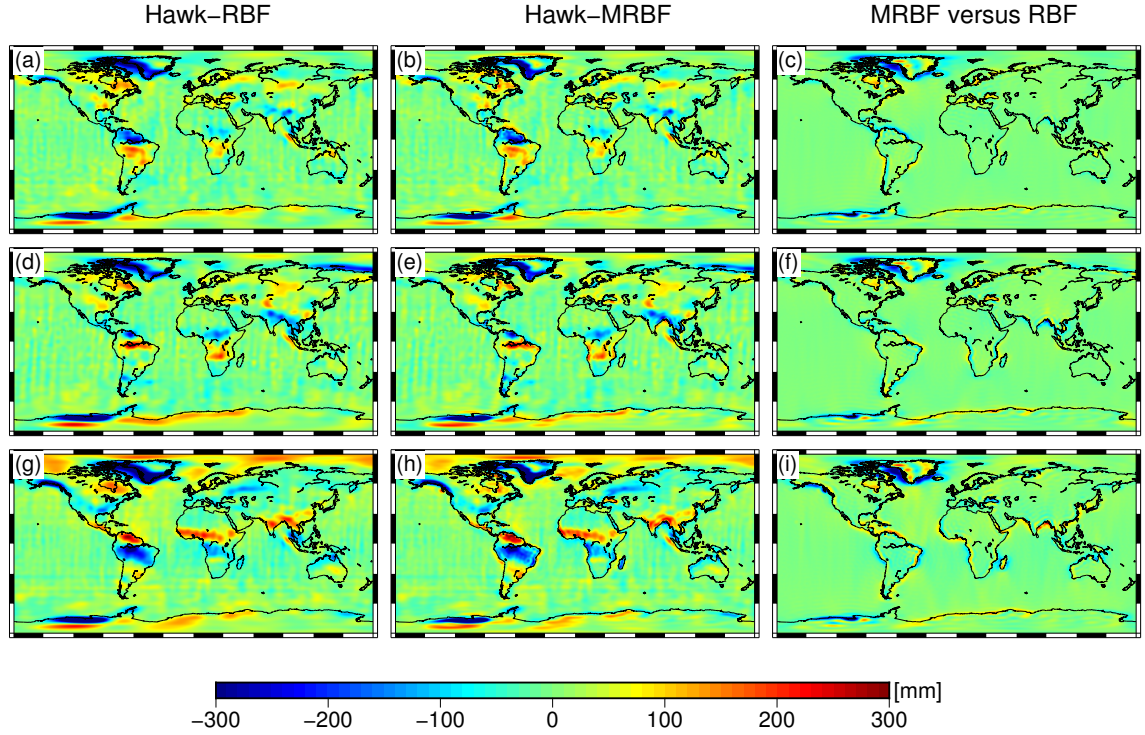452   in 72 months (from Jan 2005 to Dec 2010) is selected as a measure of the noise level, since we expect

Figure 8. Mass anomaly in terms of EWH: (a) *Hawk*-RBF on January 2010; (b) *Hawk*-MRBF on January 2010; (c) *Hawk*-MRBF versus *Hawk*-RBF on January 2010; (d) *Hawk*-RBF on May 2010; (e) *Hawk*-MRBF on May 2010; (f) *Hawk*-MRBF versus *Hawk*-RBF on May 2010; (g) *Hawk*-RBF on September 2010; (h) *Hawk*-MRBF on September 2010; (i) *Hawk*-MRBF versus *Hawk*-RBF on September 2010.

that here the hydrological signal is less dominate. And the results show that the respective RMS for the filtered SH (GFZ RL05a, *Hawk*-SH) and regularized (M)RBF (*Hawk*-RBF, *Hawk*-MRBF) are close to each other: 1.10 *cm*, 0.87 *cm*, 0.92 *cm* and 1.02 *cm* in terms of EWH.

Figure 9 provides insight into the yearly trend maps from Jan 2005 to Dec 2010). We first compare the spectral contents of these four maps in Fig. 9(a-d), and find the correlation coefficients between GFZ RL05 and the other three models (*Hawk*-SH, *Hawk*-RBF, *Hawk*-MRBF) are 0.99, 0.92, 0.91, in terms of per-degree geoid heights before d/o 20. This indicates that large-scale trend patterns derived from these four models agree well, in another word, the long-wavelength gravity signals from these four models have been appropriately retained after the regularization or post-filtering. However, differences are still remarkable at basin scale if we carefully distinguish between the SH and (M)RBF trend maps in Figure 9. Both RBF and MRBF solutions yield a better spatial resolution than SH solutions, as evidenced by Southern Greenland, West Antarctica, Amazon, South Asia and

the Europe. The question that now arises is: does the physical constraint embedded in MRBF affect the recovered gravity signals? To address this, we assess EWH trends from Fig. 9 over a coastal area: West Antarctica. The numerical result shows that *Hawk*-MRBF improves the TWS (total water storage) trend of West Antarctica by 4% with respect to *Hawk*-RBF, and by 23% with respect to GFZ RL05a (or *Hawk*-SH). Furthermore, a visual inspection by zooming in to *Hawk*-MRBF and *Hawk*-RBF trend maps (see Fig. 11) also suggests that *Hawk*-MRBF has less leaked signals around the coasts of West Antarctica. We also mention that, another added value of *Hawk*-MRBF is that the MRBF process does not significantly affect the continental gravity signals that are far away from the coastlines, such as West China.
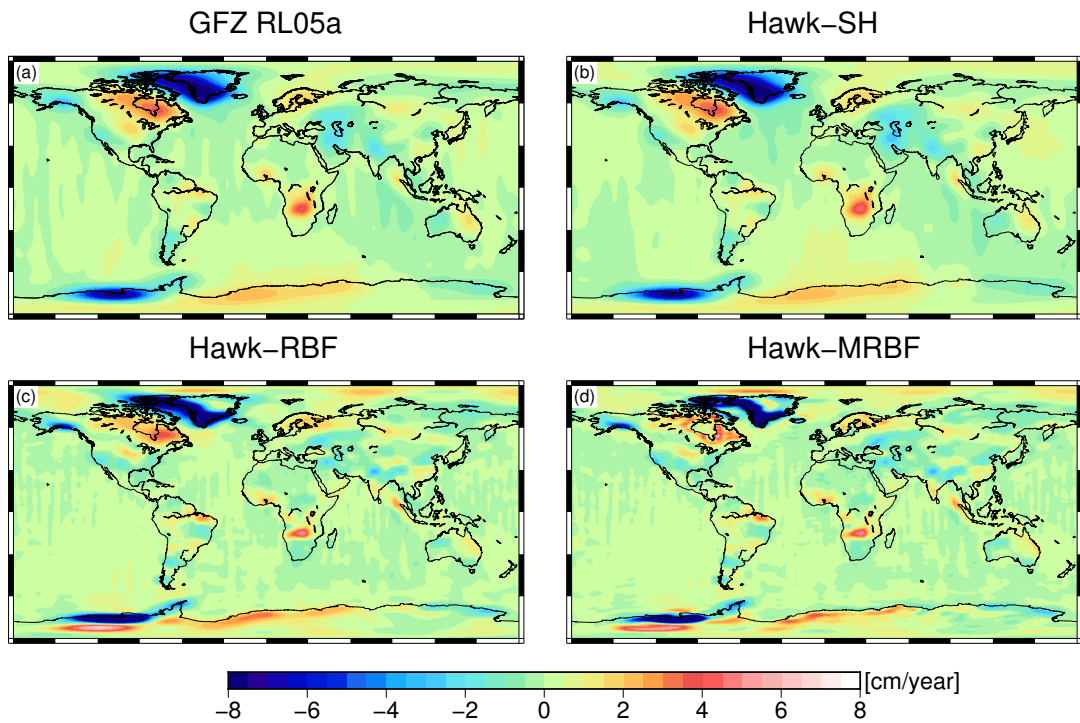

Figure 9. The 2005-2010 yearly trends derived from GFZ RL05a, *Hawk*-SH, *Hawk*-RBF and *Hawk*-MRBF products up to d/o 90, expressed in [cm/yr] of EWH.

In addition, annual amplitudes of the gravity variations are shown in Fig. 10, from which we could gain some similar findings, following that: (i) the (M)RBF solutions capture finer scale gravity changes than the SH solutions do, over the majority of the regions like Southern Greenland, Australia, Africa, Amazon and South Asia, etc. (ii) Considerable differences between *Hawk*-MRBF and *Hawk*-RBF solutions are mostly distributed along the coastlines, such as the northwestern coastline of North
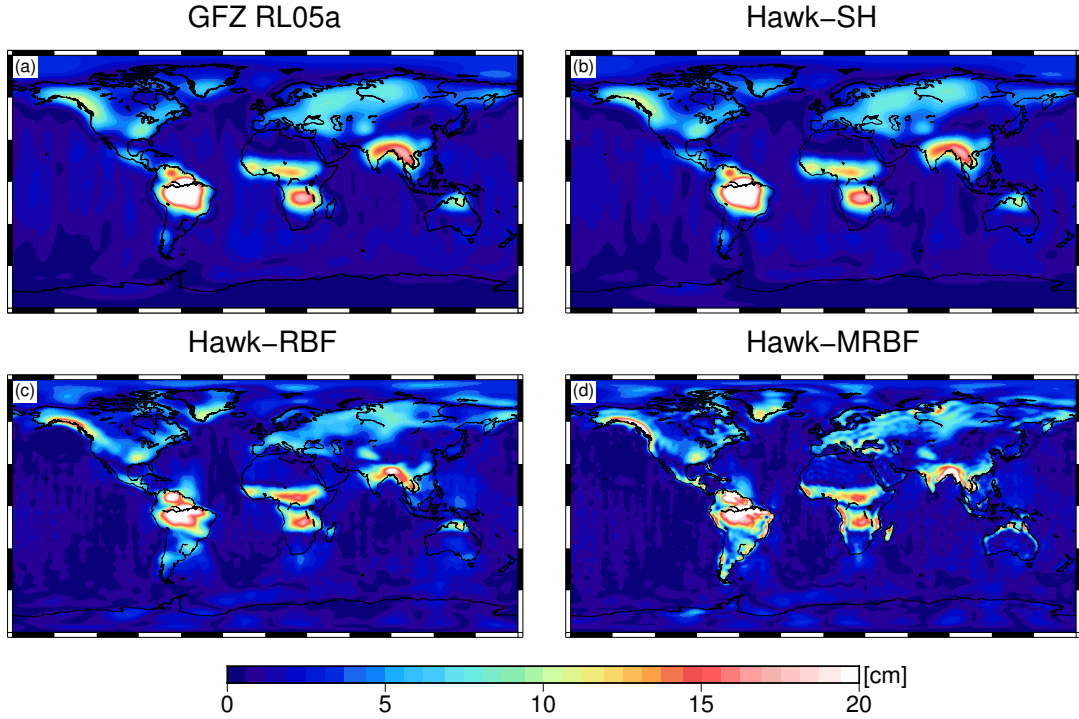
GFZ RL05a   Hawk–SH

Hawk–RBF   Hawk–MRBF

Figure 10. The 2005-2010 annual amplitudes derived from GFZ RL05a, *Hawk*-SH, *Hawk*-RBF and *Hawk*-MRBF products up to d/o 90, expressed in [cm] of EWH.

America, western coastlines of Africa, coastlines of Black Sea, Indonesia etc. To better distinguish the differences between *Hawk*-RBF and *Hawk*-MRBF, Fig. 11 illustrates an alternative zoomed-in maps of the northern Australia and South Asia areas, where users of GRACE L2 products face a significant leakage problem that was addressed in previous studies [see e.g., *Shum et al.*, 2010; *Forootan et al.*, 2012]. In these regions, the proposed MRBF solutions appear in visual inspection to have better localized continental signals as well as less oceanic leakage than the RBF and SH solutions. But more tests with independent data such as e.g. high-quality hydrology modelling and arrays of coastal ocean bottom recorders are required. This would however go beyond the scope of the paper.

It is worth mentioning that the obtained findings of (M)RBF products by far are well consistent with those of JPL RL05M mascon solution. In particular, compared to the corresponding SH solutions, Mascon [*Watkins et al.*, 2015] and MRBF estimations both indicate a better spatial resolution and stronger signals at these regions, for instance, at northwestern coast of North America,

at the southwestern coast of South America, over Africa and India etc. This is not a coincidence but

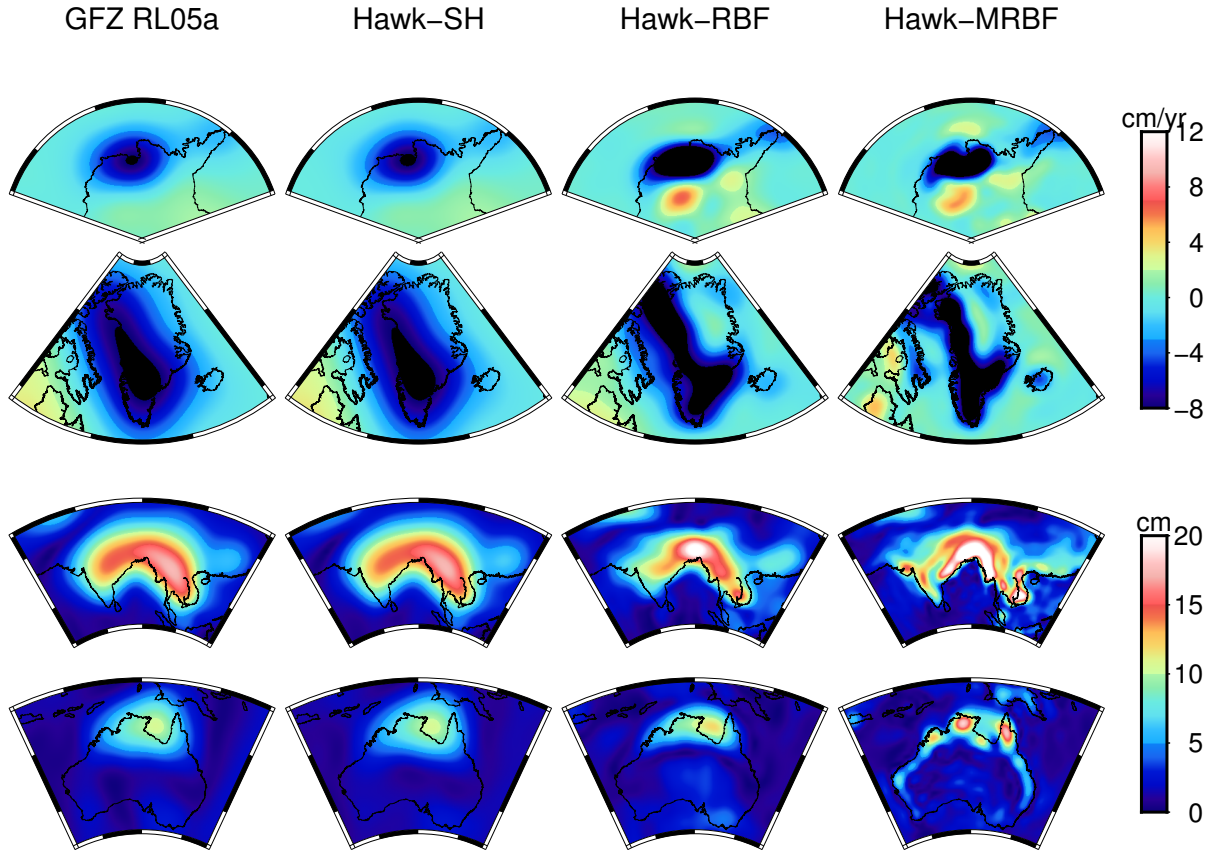probably due to the particular treatment of the spatial leakage embedded in the inversion.

Figure 11. From left to right, the 2005-2010 derived signals that are expressed in [cm/yr] of EWH for GFZ RL05a, *Hawk*-SH, *Hawk*-RBF and *Hawk*-MRBF up to d/o 90, respectively. Row 1 and Row 2 respectively represent the trend patterns over Greenland and Antarctica; Row 3 and Row 4 indicate the annual amplitude patterns over South Asia and Australia, respectively.

In the following, we illustrate the zoomed-in signals over four selected regions as shown in Fig. 11, with however a major focus on Greenland. This polar glacier region has been frequently pointed out that its mass-loss estimates suffer from a severe spatial leakage [see, e.g. *Velicogna and Wahr*, 2013; *Velicogna et al.*, 2014], as the majority of ice-melting is taking place along the coastal regions. Therefore, a set of scale factors [*Baur et al.*, 2009] up to 1 ~ 2 is usually applied to rescale the mass loss estimates in Greenland, but this is not used in our study. Here, we present the time series of gravity changes in terms of TWS over the Southern Greenland (below Lat 70°, a major ice-melting
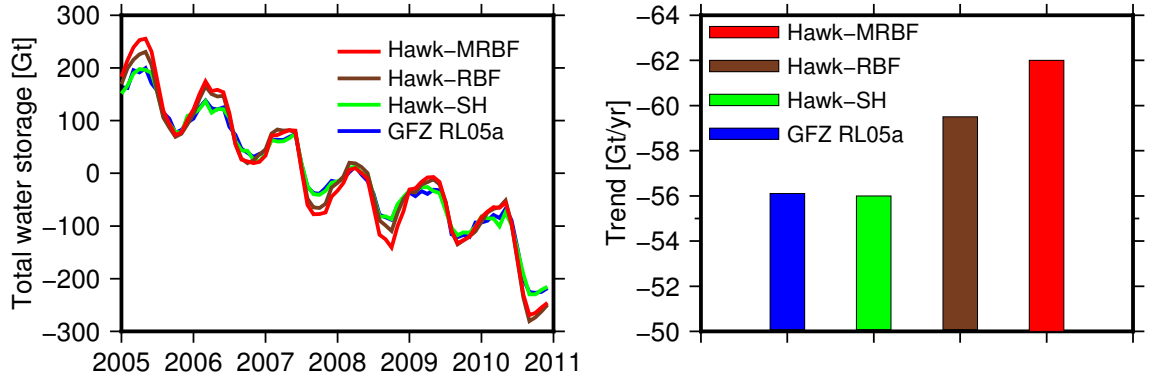
Figure 12. Left panel represents the 2005-2010 monthly TWS over Southern Greenland (below Lat 70°) for GFZ RL05, *Hawk*-SH, *Hawk*-RBF and *Hawk*-MRBF; Right panel is the respective statistic of yearly trend for each model.

region), for SH and (M)RBF models in Fig. 12 (left). The red and the brown curves are obviously more steep than the green and the blue, and this indicates that the (M)RBF might have a larger yearly trend and therefore lower the dependence on using scale factors. The statistical yearly trends for GFZ RL05a, *Hawk*-SH, *Hawk*-RBF and *Hawk*-MRBF are -56.1 Gt/yr, -56.0 Gt/yr, -59.5 Gt/yr and -62 Gt/yr in terms of TWS, which are also shown in Fig. 12 (right). The MRBF has considerably improved the mass loss estimates by almost 11% during 2005-2010 when compared to SH solutions, and we attribute this progress to our regional basis functions that better exploit the rich high-latitude distribution of GRACE observations. Furthermore, the trend estimated from MRBF solutions is found to be only 4% bigger than that of RBF. An alternative experiment of yearly trend estimate (not shown here) is performed over the entire Greenland, and the result demonstrates that the difference between trends of the RBF and MRBF solutions increases to 6% approximately without accounting for Glacial Isostatic Adjustment (GIA) or any other corrections. The magnitude of the differences might seem small, but it should not be ignored. In this context, the spatial leakage still contaminates the MRBF solution, such that it also needs scale factors for providing an accurate mass estimate like JPL RL05M mascon solution. The potential causes could be (i) the network geometric together with the finite shape kernel within MRBFs contains an implicit spatial average that is unavoidable, and (ii) the applied extra Gaussian filter with the radius of 200km introduces the additional spatial leakage. However, quantifying the MRBF's leakage reduction with in situ or other independent measurements will be more reliable, and this will be subject to future investigations.

6 Conclusions and outlook

This paper presents a set of non-isotropic self-consistent MRBF bases, which are similar to RBFs but they impose the additional constraints of mass-conservation and passive ocean response (Sec. 2). Prior to implementing MRBFs in GRACE L1b inversion, the data processing chain in our in-house software was briefly introduced and validated by comparing the in-house SH-based gravity field against those provided by the official centers (Sec. 3). We further calculated the time series of gravity fields from GRACE observations in terms of RBF and MRBF, respectively. In Section 4, a case study on May 2009 was carried out and demonstrated that both RBF and MRBF are comparable to SH-based solutions unless the regularization is applied. There, it was also revealed that the MBRF solution could achieve an accurate gravity estimate with a smaller amount of basis functions participated in the inversion procedures, leading to a dimension reduction of estimated parameters and a speed-up of the numerical calculation (Sec. 4.1). This case study also suggests that the MRBF solutions indicate stronger numerical stability during the regularization, due to the lower dependence between the oceanic and continental signals (Sec. 4.2). In Section 5, after analyzing the annual amplitude and trend maps derived from the time series of (M)RBF and SH gravity fields, it was shown that the MRBF solution improves the gravity recovery at coastal regions in terms of both spatial resolution and magnitude, hinting that a more accurate modelling of coastal gravity signals could be expected.

Despite the demonstrated advances already obtained by applying the self-consistent MRBF representation, there is still potential for further improvements of this approach in the following aspects: (i) Besides the proposed MRBF-I in this study, an complementary set of MRBF-II could be developed to treat with another type of spatial leakage from ocean to land (not considered by MRBF-I), and we hope in this way the leakage could be further reduced. (ii) Another improvement in accuracy could be expected by applying a more appropriate regularization tailored to the reliable a-priori geophysical information. This will well minimize the striping error without the necessity of applying additional spatial averaging in a post-processing step. (iii) The original RBF that we use here to develop MRBF is shaped by a Shannon kernel and consequently has a smooth spectrum, but together with a strong spatial oscillation. This might be replaced by another type of RBF (e.g. wavelet or Poisson RBF, or the very popular Mascons) that has a smooth spatial performance so as to construct a new set of MRBFs, which will further reduce the spatial leakage and advance the resolution of coastal gravity recovery.

Acknowledgments

References

Baur, O., and N. Sneeuw (2011), Assessing Greenland ice mass loss by means of point-mass modeling: a viable methodology, *Journal of Geodesy*, *85*(9), 607–615.

Baur, O., M. Kuhn, and W. Featherstone (2009), GRACE-derived ice-mass variations over Greenland by accounting for leakage effects, *Journal of Geophysical Research: Solid Earth*, *114*(B6).

Bentel, K., M. Schmidt, and C. Gerlach (2013), Different radial basis functions and their applicability for regional gravity field representation on the sphere, *GEM-International Journal on Geomathematics*, *4*(1), 67–96.

Bettadpur, S. (2009), Recommendation for a-priori bias and scale parameters for Level-1B ACC data (version 2), *GRACE TN-02*.

Bettadpur, S. (2012), Insights into the Earth system mass variability from CSR-RL05 GRACE gravity fields, in *EGU General Assembly Conference Abstracts*, vol. 14, p. 6409.

Beutler, G., A. Jäggi, L. Mervart, and U. Meyer (2010), The celestial mechanics approach: application to data of the GRACE mission, *Journal of Geodesy*, *84*(11), 661–681.

Blewitt, G., and P. Clarke (2003), Inversion of Earth's changing shape to weigh sea level in static equilibrium with surface mass redistribution, *Journal of Geophysical Research: Solid Earth*, *108*(B6).

Blewitt, G., P. Clarke, D. Lavallée, and K. Nurutdinov (2005), Application of Clebsch-Gordan coefficients and isomorphic frame transformations to invert Earth's changing geometrical shape for continental hydrological loading and sea level′s passive response, in *A Window on the Future of Geodesy*, pp. 518–523, Springer.

Bruinsma, S., J.-M. Lemoine, R. Biancale, and N. Valès (2010), CNES/GRGS 10-day gravity field models (release 2) and their evaluation, *Advances in Space Research*, *45*(4), 587–601.

Case, K., G. Kruizinga, and S. Wu (2002), GRACE level 1B data product user handbook, *JPL Publication D-22027*.

Chen, J., C. Wilson, and B. Tapley (2006), Satellite gravity measurements confirm accelerated melting of Greenland ice sheet, *Science*, *313*(5795), 1958–1960.

Clarke, P. J., D. A. Lavallée, G. Blewitt, T. Van Dam, and J. Wahr (2005), Effect of gravitational consistency and mass conservation on seasonal surface mass loading models, *Geophysical Research Letters*, *32*(8).

Clarke, P. J., D. A. Lavallée, G. Blewitt, and T. Van Dam (2007), Basis functions for the consistent and accurate representation of surface mass loading, *Geophysical Journal International*, *171*(1), 1–10.

Dahle, C., F. Flechtner, C. Gruber, D. König, R. König, G. Michalak, and K.-H. Neumayer (2014), GFZ RL05: An improved time-series of monthly GRACE gravity field solutions, in *Observation of the System Earth from Space-CHAMP, GRACE, GOCE and future missions*, pp. 29–39, Springer.

Dahlen, F. (1976), The passive influence of the oceans upon the rotation of the Earth, *Geophysical Journal International*, *46*(2), 363–406.

Eicker, A. (2008), Gravity field refinement by radial basis functions from in-situ satellite data, Ph.D. thesis, University of Bonn.

Eicker, A., J. Schall, and J. Kusche (2013), Regional gravity modelling from spaceborne data: case studies with GOCE, *Geophysical Journal International*, *196*(3), 1431–1440.

Flechtner, F., H. Dobslaw, and E. Fagiolini (2013), AOD1b product description document for product release 05, *GFZ German Research Centre for Geosciences*.

Forootan, E., J. Awange, J. Kusche, B. Heck, and A. Eicker (2012), Independent patterns of water mass anomalies over australia from satellite data and models, *Remote Sensing of Environment*, *124*, 427–443

Gunter, B., T. Wittwer, W. Stolk, R. Klees, and P. Ditmar (2012), Comparison of regional and global GRACE gravity field models at high latitudes, in *Geodesy for Planet Earth*, pp. 171–177, Springer.

Jekeli, C. (1981), Alternative methods to smooth the Earth's gravity field, *Tech. rep.*, Ohio State Univ.

Kang, Z., B. Tapley, S. Bettadpur, and H. Save (2009), Quality of GRACE orbits using the reprocessed IGS products, in *AGU Fall Meeting Abstracts*, vol. 1, p. 05.

Keller, W. (2004), *Wavelets in geodesy and geodynamics*, Walter de Gruyter.

Kim, J. (2000), Simulation study of a low-low satellite-to-satellite tracking mission, Ph.D. thesis, The University of Texas at Austin.

Klees, R., X. Liu, T. Wittwer, B. Gunter, E. Revtova, R. Tenzer, P. Ditmar, H. Winsemius, and H. Savenije (2008), A comparison of global and regional GRACE models for land hydrology, *Surveys in Geophysics*, *29*(4-5), 335–359

Koch, K.-R., and J. Kusche (2002), Regularization of geopotential determination from satellite data by variance components, *Journal of Geodesy*, *76*(5), 259–268.

Kusche, J. (2007), Approximate decorrelation and non-isotropic smoothing of time-variable GRACE-type gravity field models, *Journal of Geodesy*, *81*(11), 733–749.

Kusche, J., and R. Klees (2002), Regularization of gravity field estimation from satellite gravity gradients, *Journal of Geodesy*, *76*(6-7), 359–368.

Kusche, J., V. Klemann, and W. Bosch (2012), Mass distribution and mass transport in the Earth system, *Journal of Geodynamics*, *59*, 1–8.

Landerer, F., and S. Swenson (2012), Accuracy of scaled GRACE terrestrial water storage estimates, *Water Resources Research*, *48*(4).

Long, D., Y. Yang, Y. Wada, Y. Hong, W. Liang, Y. Chen, B. Yong, A. Hou, J. Wei, and L. Chen (2015), Deriving scaling factors using a global hydrological model to restore GRACE total water storage changes for China's yangtze river basin, *Remote Sensing of Environment*, *168*, 177–193.

Luthcke, S. B., H. Zwally, W. Abdalati, D. Rowlands, R. Ray, R. Nerem, F. Lemoine, J. McCarthy, and D. Chinn (2006), Recent Greenland ice mass loss by drainage system from satellite gravity observations, *Science*, *314*(5803), 1286–1289.

Luthcke, S. B., T. Sabaka, B. Loomis, A. Arendt, J. McCarthy, and J. Camp (2013), Antarctica, Greenland and Gulf of Alaska land-ice evolution from an iterated GRACE global mascon solution, *Journal of Glaciology*, *59*(216), 613–631.

Naeimi, M. (2013), Inversion of satellite gravity data using spherical radial base functions, Ph.D. thesis, Fachrichtung Geodäsie und Geoinformatik der Leibniz Universität Hannover.

Petit, G., and B. Luzum (2010), IERS conventions 2010. International earth rotation and reference systems service, *Tech. rep.*, IERS Technical Note.

Rasch, J., and A. Yu (2004), Efficient storage scheme for precalculated Wigner 3 j, 6 j and Gaunt coefficients, *SIAM Journal on Scientific Computing*, *25*(4), 1416–1428.

Ries, J., S. Bettadpur, S. Poole, and T. Richter (2011), Mean background gravity fields for GRACE processing, in *GRACE science team meeting, Austin, TX*, pp. 8–10.

Rowlands, D., S. Luthcke, J. McCarthy, S. Klosko, D. Chinn, F. Lemoine, J.-P. Boy, and T. Sabaka (2010), Global mass flux solutions from GRACE: a comparison of parameter estimation strategies-mass concentrations versus Stokes coefficients, *Journal of Geophysical Research: Solid Earth*,

115(B1).

Sadourny, R., A. Arakawa, and Y. Mintz (1968), Integration of the nondivergent barotropic vorticity equation with an icosahedral-hexagonal grid for the sphere, *Monthly Weather Review*, *96*(6), 351–356.

Savcenko, R., and W. Bosch (2012), EOT11a-empirical ocean tide model from multi-mission satellite altimetry.

Save, H., S. Bettadpur, and B. D. Tapley (2012), Reducing errors in the GRACE gravity solutions using regularization, *Journal of Geodesy*, *86*(9), 695–711.

Save, H. V. (2009), Using regularization for error reduction in GRACE gravity estimation, Ph.D. thesis, University of Texas at Austin.

Schmidt, M., O. Fabert, and C. Shum (2005), On the estimation of a multi-resolution representation of the gravity field based on spherical harmonics and wavelets, *Journal of Geodynamics*, *39*(5), 512–526.

Schmidt, M., M. Fengler, T. Mayer-Gürr, A. Eicker, J. Kusche, L. Sánchez, and S.-C. Han (2007), Regional gravity modeling in terms of spherical base functions, *Journal of Geodesy*, *81*(1), 17–38.

Schmidt, R., P. Schwintzer, F. Flechtner, C. Reigber, A. Güntner, P. Döll, G. Ramillien, A. Cazenave, S. Petrovic, H. Jochmann, et al. (2006), GRACE observations of changes in continental water storage, *Global and Planetary Change*, *50*(1), 112–126.

Shum, C., J.-Y. Guo, F. Hossain, J. Duan, D. E. Alsdorf, X.-J. Duan, C.-Y. Kuo, H. Lee, M. Schmidt, and L. Wang (2010), Inter-annual water storage changes in asia from GRACE data, in *Climate Change and Food Security in South Asia*, pp. 69–83, Springer

Spada, G., and P. Stocchi (2007), Selen: A Fortran 90 program for solving the sea-level equation, *Computers & Geosciences*, *33*(4), 538–562.

Standish, E. (1995), The JPL planetary and lunar ephemerides DE402/LE402, in *Bulletin of the American Astronomical Society*, vol. 27, p. 1203.

Swenson, S., and J. Wahr (2006), Post-processing removal of correlated errors in GRACE data, *Geophysical Research Letters*, *33*(8).

Tapley, B. D., S. Bettadpur, M. Watkins, and C. Reigber (2004), The gravity recovery and climate experiment: Mission overview and early results, *Geophysical Research Letters*, *31*(9).

Tikhonov, A., and V. Y. Arsenin (1977), *Methods for solving ill-posed problems*, John Wiley and Sons, Inc.

Velicogna, I., and J. Wahr (2013), Time-variable gravity observations of ice sheet mass balance: Precision and limitations of the GRACE satellite data, *Geophysical Research Letters*, *40*(12),

3055–3063.

Velicogna, I., T. Sutterley, and M. Van den Broeke (2014), Regional acceleration in ice mass loss from Greenland and Antarctica using GRACE time-variable gravity data, *Geophysical Research Letters*, *41*(22), 8130–8137.

Wahr, J., M. Molenaar, and F. Bryan (1998), Time variability of the earth's gravity field: Hydrological and oceanic effects and their possible detection using GRACE, *Journal of Geophysical Research: Solid Earth*, *103*(B12), 30,205–30,229.

Wang, H., L. Xiang, L. Jia, L. Jiang, Z. Wang, B. Hu, and P. Gao (2012), Load love numbers and Green's functions for elastic Earth models PREM, iasp91, ak135, and modified models with refined crustal structure from Crust 2.0, *Computers & Geosciences*, *49*, 190–199.

Watkins, M. M., and D.-N. Yuan (2012), JPL Level-2 Processing Standards Document For Level-2 Product Release 05.

Watkins, M. M., D. N. Wiese, D.-N. Yuan, C. Boening, and F. W. Landerer (2015), Improved methods for observing Earth's time variable mass distribution with GRACE using spherical cap mascons, *Journal of Geophysical Research: Solid Earth*, *120*(4), 2648–2671.

Wittwer, T. (2009), Regional gravity field modelling with radial basis functions, Ph.D. thesis, TU Delft, Delft University of Technology.

Wouters, B., J. Bonin, D. Chambers, R. Riva, I. Sasgen, and J. Wahr (2014), GRACE, time-varying gravity, Earth system dynamics and climate change, *Reports on Progress in Physics*, *77*(11), 116,801.